Cement and Concrete Research 96 (2017) 1–12

Contents lists available at ScienceDirect

Cement and Concrete Research

journal homepage: www.elsevier.com/locate/cemconres

Aluminum hydroxide gel characterization within a calcium aluminate cement paste by combined Pair Distribution Function and Rietveld analyses

Ana Cuesta [a,*], Rodrigo U. Ichikawa [b], Diana Londono-Zuluaga [c], Angeles G. De la Torre [c], Isabel Santacruz [c], Xavier Turrillas [a,d], Miguel A.G. Aranda [a,c]

[a] ALBA Synchrotron, Carrer de la Llum, 2-26, E-08290 Cerdanyola del Vallés, Barcelona, Spain
[b] IPEN-Instituto de Pesquisas Energéticas e Nucleares, Av. Prof. Lineu Prestes, 2242 - Cidade Universitária, São Paulo, SP, 05508-000, Brazil
[c] Departamento de Química Inorgánica, Universidad de Málaga, Campus Teatinos S/N, 29071 Málaga, Spain
[d] Institut de Ciència de Materials de Barcelona – CSIC, UAB Campus, 08193 Cerdanyola del Vallès, Barcelona, Spain

ARTICLE INFO

Article history:
Received 18 November 2016
16 February 2017
Accepted 24 February 2017
Available online 19 March 2017

Keywords:
X-ray diffraction (B)
Calcium aluminate cement (D)
Hydrogarnet (D)
Amorphous material (A)
Aluminum hydroxide gel (D)

ABSTRACT

There are many commercially important multiphase materials which contain amorphous phases, such as cement pastes, porcelains, glass-ceramics or pharmaceutical compounds. However, the analysis of amorphous phase(s) within cement matrices that contain high amounts of crystalline phase(s) is a challenge. Here, we report measurements of total scattering data quantitatively analyzed by Pair Distribution Function (PDF) minimization and Rietveld methodology to determine phase compositions including both amorphous and nanocrystalline phase contents in cement-related samples. Furthermore, laboratory techniques were used to complement the sample characterization. In addition to five reference materials, the main phase of calcium aluminate cements, $CaA_{l2}O_4$ hydrated at 50 °C to yield crystalline hydrogarnet, $Ca_3Al_2(OH)_{12}$, (43 wt%) and nanocrystalline aluminum hydroxide gel, $Al(OH)_3 \cdot 0.1H_2O$ (50 wt%) was also investigated. The PDF analyses revealed that the hydroxide gel has a gibbsite local structure with an average particle size close to 5 nm. PDF and Rietveld quantitative phase analysis results fully agree.

1. Introduction

Crystalline, nanocrystalline and amorphous $Al(OH)_3$ materials are important in a number of fields including the aluminum production by the Bayer process, some types of cements, flocculants in water purification, antacid in medicine, precursors for catalysts, anti-flame additive for polymers, and so on. Gibbsite, doyleite, nordstrandite and bayerite are the four known polymorphs of crystalline $Al(OH)_3$ belonging to the wider family of water-containing aluminum oxides including amorphous compounds [1–4].

The characterization of both nanocrystalline and amorphous materials is challenging, but their analysis in samples containing large amounts of crystalline materials is even more difficult. At this point it is important to clarify the differences between nanocrystalline and amorphous phases. In a nanocrystalline phase, the atomic structure can be described to a good approximation by using the crystal structure truncated in the real space by a nanosized shape function. Finite models that take into account surface relaxation effects may be employed. Conversely, an amorphous compound cannot be properly described by using a truncated crystal structure [5].

Regarding calcium aluminate cement hydration, amorphous/nanocrystalline aluminum hydroxide coexists with other crystalline materials as a result of the hydration reactions [6]. For instance, $CaAl_2O_4$ is the main phase of calcium aluminate cements [6] and its hydration mechanism has been widely studied [6–9]. The mechanism of this hydration reaction strongly depends on temperature, as different crystalline phases can be formed with temperature [10]. For temperatures lower than 15 °C it hydrates according to reaction (1) where no gel is formed.

$$CaAl_2O_4 + 10H_2O \rightarrow CaAl_2O_4 \cdot 10H_2O \quad (1)$$

At intermediate temperatures, between 15 and 30 °C, $CaAl_2O_4$ hydrates according to reactions (2) and (3).

$$3CaAl_2O_4 + (21 + 2n)H_2O \rightarrow CaAl_2O_4 \cdot 10H_2O + Ca_2Al_2O_5 \cdot 8H_2O + 2\left[Al(OH)_3 \cdot nH_2O\right] \quad (2)$$

$$2CaAl_2O_4 + (11 + 2n)H_2O \rightarrow Ca_2Al_2O_5 \cdot 8H_2O + 2\left[Al(OH)_3 \cdot nH_2O\right] \quad (3)$$

At temperatures higher than 30 °C, $CaAl_2O_4$ hydrates according to reaction (4) to give hydrogarnet, $Ca_3Al_2(OH)_{12}$ and aluminum

* Corresponding author.
E-mail address: acuesta@cells.es (A. Cuesta).

http://dx.doi.org/10.1016/j.cemconres.2017.02.025
0008-8846/

hydroxide gel [8].

$$3CaAl_2O_4 + (12 + 4n)H_2O \rightarrow Ca_3Al_2(OH)_{12} + 4\left[Al(OH)_3 \cdot nH_2O\right] \quad (4)$$

Calcium aluminate cements (CAC) are currently used for special applications. Some of their main advantages are: high early strength development, high chemical resistance, workability at low temperatures and rapid strength development at low temperatures [6]. However, the use of CAC for concrete manufacture became highly controversial after some incidents occurred mainly in the United Kingdom and Spain. The complex evolution of this material, under some environmental conditions, is still not fully understood and it may lead to collapses. $CaAl_2O_4 \cdot 10H_2O$ slowly transforms into hydrogarnet jointly with aluminum hydroxide gel and water. This conversion, whose rate depends at least on humidity and temperature, could be completed within several years. This causes an increase in concrete porosity and a loss of strength. Moreover, chemical reactions facilitated by the porosity can cause a continuous loss of strength [11].

The crystal structure of the crystalline component, $Ca_3Al_2(OH)_{12}$, is well known [12]. However, the chemical nature of the accompanying aluminum hydroxide gel is still to be unraveled. Related aluminum hydroxide gels are also formed in more complex systems such as the hydration of calcium sulfoaluminate cements [13–16]. The composition, including possible water content and local structure of aluminum hydroxide gels in cementitious systems is difficult to study because of its nanocrystalline/amorphous nature.

The Rietveld method has been extensively used to characterize the hydration mechanisms of calcium aluminate cements in particular [17], and of other cementitious systems in general [18–21]; however, it is worth highlighting the importance of using alternative methods for the characterization of amorphous and nanocrystalline phases. In particular, atomic Pair Distribution Function (PDF) analysis of powder diffraction data can give information about the local structure of those components [22]. This approach, using synchrotron radiation [23], has been used in the characterization of calcium-silicate-hydrate gels in cement studies [24–26]. It was found that this type of gel shows nanocrystalline ordering with coherent diffraction particle diameters close to 3.5 nm [26]. Other amorphous cementitious components such as geopolymers [26,27] and fly ash [28] have also been studied by PDF. We highlight the recent PDF study of several calcium-(aluminum)-silicate-hydrate gels [5] where the differences between nanocrystalline and amorphous phases were extensively discussed.

The PDF function, also known as G(r), shows the probability of finding pairs of atoms separated by a distance r. G(r) is experimentally obtained by a Fourier transform of the total scattering powder diffraction pattern, according to Eq. (5) [22,29,30].

$$G(r) = 4\pi r[\rho(r) - \rho_0] = \frac{2}{\pi}\int_0^\infty Q[S(Q) - 1]\,\sin(Qr)dQ \quad (5)$$

where $\rho(r)$ is the microscopic atomic pair density, ρ_0 is the average atomic number density, S(Q) is the total scattering structure function and Q is the momentum transfer [22], $Q = 4\pi\sin(\theta)/\lambda$). In order to obtain PDF patterns with very good quality, the recorded Q-range has to be large. For this reason, the use of a short wavelength and high 2θ diffracting angles is very important [31].

As in the Rietveld method, the experimental PDF data can be used to refine a structural model but only if the correct r-range is used for the calculations [30,32]. Similarly, the quantitative phase analysis of mixtures is also possible but again the correct r-range must be employed [30,31]. The phase content analyses of complex samples that usually include amorphous phases are very important and they are being currently studied in depth in pharmaceutical compounds [31,33–35].

To the best of our knowledge, there is just one paper reporting PDF data of crystalline $Al(OH)_3$ phases [36]. However, the corresponding results concerning gibbsite and bayerite were just qualitative. We are not aware of PDF studies dealing with amorphous aluminum hydroxides; there is only one report using PDF data, collected from Mo-radiation, where the local environment of nanocrystalline boehmite AlO(OH) is characterized [37]. Finally, there are some PDF studies for characterizing amorphous γ-Al_2O_3 [38,39].

This work is framed within a research project aiming to better characterize aluminum hydroxide gels formed in cement hydration (calcium aluminate, calcium sulfoaluminate, sulfobelite cements, and so on). In order to do that, we have studied five reference samples and one model specimen containing aluminum hydroxide gel. The reference materials were commercial crystalline gibbsite, ground gibbsite, commercial amorphous aluminum hydroxide, laboratory-synthesized boehmite and laboratory-synthesized hydrogarnet. The investigated sample, prepared from the hydration of $CaAl_2O_4$, contained hydrogarnet and aluminum hydroxide gel. In addition to qualitative and quantitative PDF analyses, Rietveld methodology, internal standard methodology, ^{27}Al MAS-NMR and thermal analysis techniques have also been employed for a thorough characterization of cement pastes.

2. Experimental section

2.1. Sample preparation

Six samples have been studied, five references and the hydrated specimen. (1) Gibbsite and (2) amorphous aluminum hydroxide powders were both bought from Sigma-Aldrich and used as received. (3) Crystalline gibbsite powder was attrition milled with isopropanol for 80 min (8 cycles of 10 min and 10 minute rest-time each). (4) Boehmite powder was prepared by heating the commercial gibbsite powder at 300 °C for 18 h. (5) Hydrogarnet sample, $Ca_3Al_2(OH)_{12}$, was prepared by hydrating $Ca_3Al_2O_6$, at a water-to-solid mass ratio of 1 for one week at room temperature (RT). The resulting powder was finally dried at 50 °C. $Ca_3Al_2O_6$ was synthesized by using suitable amounts of $CaCO_3$ (99.95%, Alfa-Aesar) and Al_2O_3 (99.997%, Alfa-Aesar). The mixture was preheated at 1000 °C for 6 h and ground for 15 min in an agate mortar. The resulting powder was dye pressed (20 mm diameter and 500 MPa) and heated at 1450 °C for 6 h. (6) $CaAl_2O_4$ was hydrated, at a water-to-solid mass ratio of 1 for eight days at 50 °C in order to obtain a mixture of hydrogarnet and aluminum hydroxide gel. The sample was filtrated in a Whatman system (90 mm diameter Whatman filter with a pore size of 2.5 μm on a Teflon support) and washed twice with acetone and finally with ether [40]. $CaAl_2O_4$ was prepared by using suitable amounts of $CaCO_3$ (99.95%, Alfa-Aesar) and Al_2O_3 (99.997%, Alfa-Aesar). The mixture was ground in a planetary mill (Fritsch, model Pulverisette 7, with a 45 cm^3 agate vessel containing 7 agate balls with a diameter of 15 mm) during 30 min at 200 rpm with reverse rotation. The resulting powder was heated at 1250 °C for 1 h and finally heated twice at 1300 °C for 2 h.

The reference samples can include some minor additional phases that will be reported in the result section.

2.2. Thermal analysis

Differential thermal analysis (DTA) and thermogravimetric (TGA) measurements were performed in a SDT-Q600 analyzer from TA instruments (New Castle, DE). A selected sample, commercial amorphous $Al(OH)_3$, was also studied in a TGA/DSC 1 analyzer from Mettler Toledo (Switzerland) which is connected to a mass spectrometer (Pfeiffer Vacuum, model Thermostar) in the exhaust gasses. In all cases, the temperature was varied from RT to 1000 °C at a heating rate of 10 °C/min. Measurements were carried out in open platinum crucibles under nitrogen flow. The weighed loss from RT to 700 °C was considered to be water and that from 700 to 1000 °C was considered as CO_2, see Table S1 provided as supporting information.

2.3. Synchrotron X-ray powder diffraction (SXRPD)

SXRPD data were collected in Debye-Scherrer (transmission) mode using the X-ray powder diffraction endstation of BL04-MSPD beamline at ALBA synchrotron (Barcelona, Spain) [41]. The wavelength, 0.41286(3) Å, was selected with a double-crystal Si (111) monochromator and determined from a Si640d NIST standard (a = 5.43123 Å) measurement. The diffractometer is equipped with a MYTHEN detector especially suited for time-resolved and extremely good signal-to-noise ratio experiments. The glass capillaries, 0.7 mm of diameter, were rotated at 20 rpm during data collection to improve diffracting particle statistics. The data acquisition time was 30 min per each individual pattern. Several patterns were collected for each sample and added in order to improve the signal-to-noise ratio in the large recorded angular range, 1 to 120° (2θ). No changes between individual patterns were observed. The overall data acquisition times ranged between 2 and 5 h.

2.4. Laboratory X-ray powder diffraction (LXRPD) and internal standard

LXRPD data were collected on a D8 ADVANCE (Bruker AXS) diffractometer (SCAI – Universidad de Malaga) equipped with a Johansson monochromator, using strictly monochromatic Mo-Kα_1 radiation, $\lambda = 0.7093$ Å, in transmission geometry (θ/θ). Samples were mixed with 20 wt% of α-Al_2O_3 (AlfaAesar 42571) as internal standard. α-Al_2O_3 was previously heated up to 1500 °C for 20 h and sieved <125 μm.

The non-crystalline content (amorphous and nanocrystalline) of the samples was determined by internal standard methodology [42] from LXRPD data.

2.5. Rietveld data analysis

Rietveld analyses were performed using the GSAS suite of programs and the EXPGUI graphic interface [43]. Final global optimized parameters were: background coefficients, zero-shift error, cell parameters, and peak shape parameters using a pseudo-Voigt function. The atomic positional coordinates and isotropic atomic displacement parameters (ADPs) for gibbsite, boehmite and hydrogarnet were optimized in their corresponding patterns.

2.6. PDF data analysis

PDF experimental data were obtained using PDFgetX3 [44] with $Q_{max} = 25$ Å^{-1}. Quantitative phase analysis information was obtained from the PDF data by using the PDFgui software [45]. Final global optimized parameters were: scale factors, cell parameters, ADPs (for high content phases), and delta2 (low-r correlated motion peak sharpening factor) [46,47] parameters. Moreover, spdiameter, the diameter of the nanoparticle, was also optimized for the nanocrystalline phases. The instrumental parameters were obtained by measuring a similar data set for crystalline nickel. Nickel PDF data analysis converged to $Q_{damp} = 0.0036$ Å^{-1} and $Q_{broad} = 0.0080$ Å^{-1}.

2.7. NMR study

^{27}Al MAS-NMR (magic angle spinning nuclear magnetic resonance) spectra were recorded at RT in an AVANCEIII HD 600 (Bruker AXS) spectrometer using a trigamma MAS probe of 2.5 mm at a spinning rate of 15 kHz. The magnetic field was 14.1 T corresponding to a ^{27}Al resonance frequency of 156.37 MHz. The ^{27}Al chemical shifts are referenced to 1 M $Al(NO_3)_3$ aqueous solution. ^{27}Al MAS NMR spectra were recorded with a short excitation pulse (1 μs corresponding to π/12 flip angle) with ^{1}H decoupling and summing up 200 scans.

2.8. TEM-EDS analysis

High resolution transmission electron microscopy (HRTEM) measurements were carried out using a FEI Talos F200X microscope equipped with X FEG and super-X EDS system with four silicon drift detectors (SDDs) which operates at an accelerating voltage of 200 kV. Spectra were collected in Scanning TEM (STEM) mode. The calcium aluminate hydrated sample was placed on a 200 mesh copper grid coated with formvar and carbon.

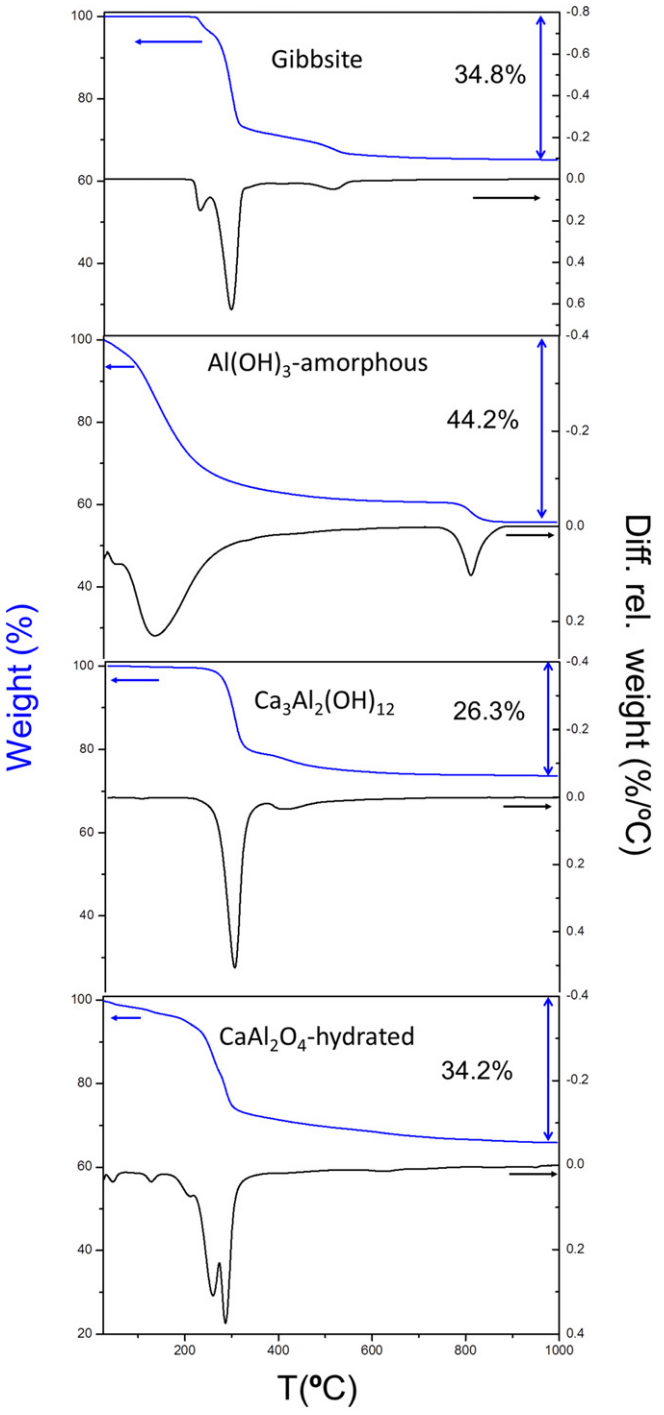

Fig. 1. Thermogravimetric data for gibbsite, amorphous $Al(OH)_3$, $Ca_3Al_2(OH)_{12}$ and $CaAl_2O_4$-hydrated.

2.9. Helium pycnometry

Helium pycnometry characterization was performed using an AccuPyc II 1340 Pycnometer (Micromeritics). The system contains a chamber of 10 cm^3 where the sample, ~3 g, is placed. The measurements were carried out at room temperature under a Helium flow of 1.34×10^5 Pa.

3. Results

3.1. Thermal analysis

The thermogravimetric data of three of the reference materials and the hydrated paste are shown in Fig. 1. The top panel of Fig. 1 displays the thermal data for crystalline gibbsite. The temperature for the main water loss step is located at 295 °C which correspond to the dehydration of gibbsite to form χ-Al_2O_3. Two additional small signals appear at 230 and 515 °C which correspond to the reactions of gibbsite to form boehmite and boehmite to yield γ-Al_2O_3, respectively [48]. The overall measured weight loss for $Al(OH)_3$ is 34.8 wt%, being 34.4 wt% from RT up to 700 °C. These weight losses are in very good agreement with the expected theoretical water loss to give aluminum oxide, 34.6 wt%.

Fig. 1 also shows the thermogravimetric data of the commercial amorphous aluminum hydroxide powder. The overall measured weight loss was 44.2 wt%. The weight loss from RT to 700 °C was 39.4 wt%, see Table S1, where the main loss is spread over a wide range, between 100 and 200 °C. A second thermal analysis using mass spectroscopy in the exhausted gasses indicated that the chemical species released above 700 °C has an atomic mass of 44 and therefore it is identified as CO_2. Under the assumption that all the weight loss below 700 °C is water and that the full mass is aluminum hydroxide, the derived stoichiometry of the sample must be close to $Al(OH)_3 \cdot 0.4H_2O$ with a content of amorphous $Al(OH)CO_3$ of about 12 wt%.

The thermogravimetric traces for the hydrogarnet sample are also shown in Fig. 1. The temperature for the main water loss step is located at 300 °C. There is a small signal close to 400 °C which could also correspond to the water loss of $Ca(OH)_2$ [49]. The overall measured weight

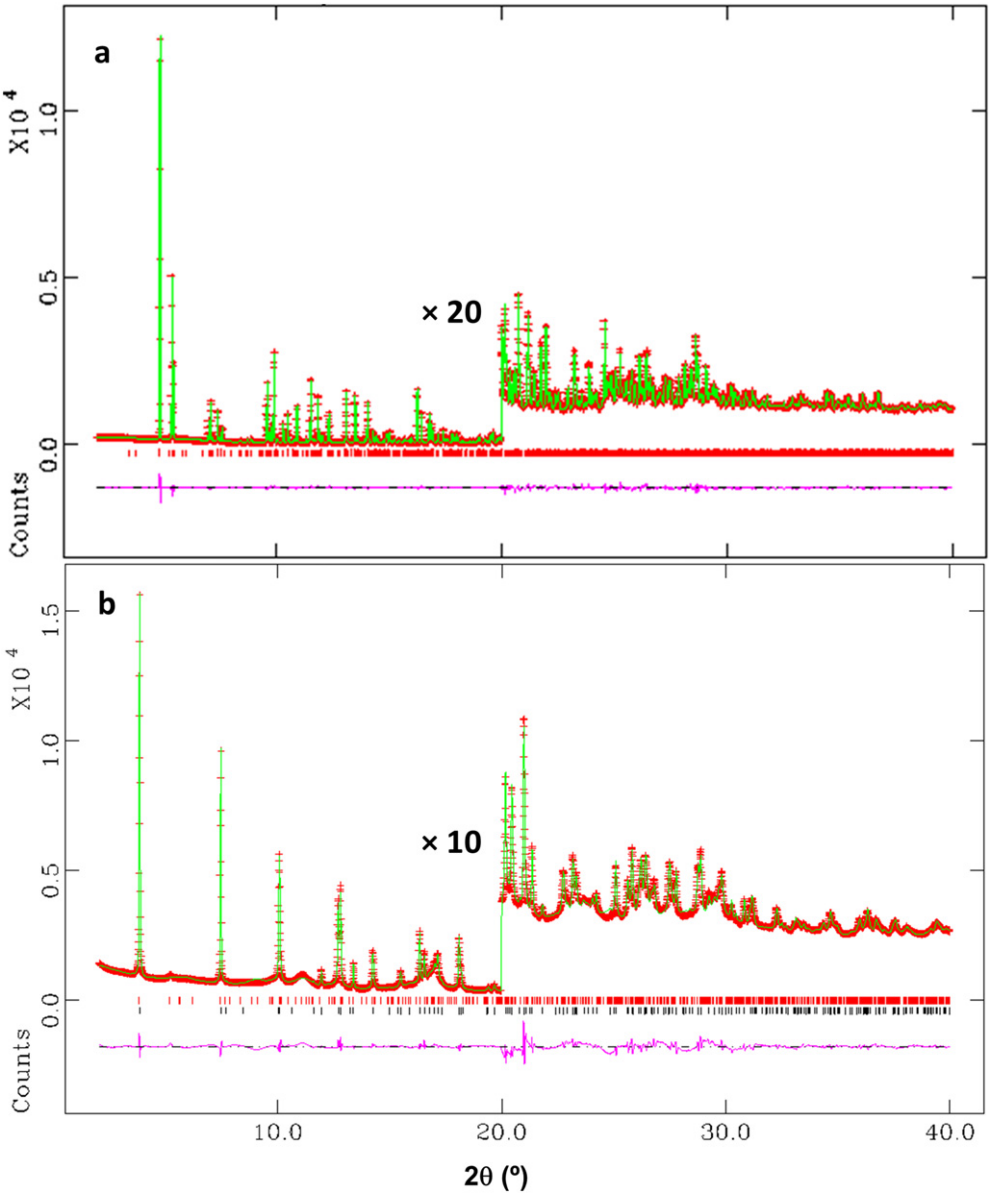

Fig. 2. SXRPD Rietveld plots (λ ~0.41 Å) for (a) crystalline gibbsite and (b) boehmite. The high angle regions, 20–40° (2θ), have been enlarged by multiplying by a factor (shown above) for a better observation. The tic marks are the allowed Bragg reflections, in (b) black for boehmite and red for κ-Al_2O_3.

loss for the $Ca_3Al_2(OH)_{12}$ sample is 26.3 wt% while the expected theoretical water loss to yield calcium aluminate is 28.6 wt%.

Finally, Fig. 1 also displays the thermogravimetric plot for the calcium aluminate hydrated sample. The overall measured weight loss is 34.2 wt% up to 1000 °C and 32.7 wt% up to 700 °C. The temperatures for the two main water loss steps are located at 260 and 290 °C. The expected water loss depends upon the sample composition (and water content of the aluminum hydroxide gel) which will be discussed below.

3.2. Rietveld and NMR characterization

Rietveld analyses were performed for all the samples except for the commercial amorphous aluminum hydroxide specimen. The powder pattern for this sample as well as that for an empty capillary is shown in Fig. S1. In addition, commercial gibbsite has a measured density of 2.43 g/cm^3, determined by helium pycnometry, which matches very well with the theoretical crystallographic density of gibbsite, 2.40 g/cm^3. This fact, together with the absence of additional diffraction peaks, see below, indicates that this phase is pure and that the amount of amorphous phase is very low, if any. As expected, the measured density of the commercial amorphous aluminum hydroxide was much lower, 2.13 g/cm^3.

The Rietveld analysis of the SXRPD pattern for crystalline gibbsite was carried out using the crystal structure previously reported [50] as starting model. The optimized unit cell values converged to a = 8.66879(3) Å, b = 5.06913(2) Å, c = 9.72131(4) Å, β = 94.557(1)° and V = 425.836(3) Å^3. After refining the atomic parameters, the final R_{WP} and R_F values dropped to 3.1 and 2.9%, respectively. Table S2 reports the refined final atomic parameters; since the improvement in the description of the crystal structures is minor, we have not deposited the structures at the ICSD data base. However, it is worth highlighting that the quality of the powder diffraction data is high enough to allow the refinement of the hydrogen atomic positions. Fig. 2a shows the final Rietveld plot where all diffraction peaks were accounted for the gibbsite structure. A LXRPD study with internal standard methodology was also performed to determine the overall amount of amorphous and nanocrystalline material. It was found that, within the errors, this content was 0. Fig. S2a shows the LXRPD Rietveld plot for gibbsite with the peaks belonging to the internal standard starred. The ^{27}Al MAS-NMR spectrum for crystalline gibbsite is displayed in Fig. 3 which main resonance is located at 9.3 ppm as previously reported [51,52].

The Rietveld analysis of the SXRPD pattern for milled gibbsite was carried out using the gibbsite structure determined just above. The optimized unit cell values converged to a = 8.6700(1) Å, b = 5.0694(1) Å, c = 9.7202(2) Å, β = 94.529(2)° and V = 425.89(2) Å^3. The final R_{WP} and R_F values were 3.5 and 2.8%, respectively. Fig. S3 shows the final Rietveld plot where all diffraction peaks were accounted for the gibbsite structure. The most noticeable features in the pattern, compared to those of the as-received gibbsite, were broader diffraction peaks and higher background contribution.

The SXRPD pattern of boehmite, AlO(OH), was also studied by the Rietveld methodology using the crystal structure previously reported [53]. The optimized unit cell values converged to a = 3.6940(1) Å, b = 12.2383(4) Å, c = 2.8649(1) Å and V = 129.52(1) Å^3. The final R_{WP} and R_F values were 4.6 and 1.8%, respectively. Table S3 reports the refined final atomic parameters. Fig. 2b shows the final Rietveld plot. It is important to highlight that the dehydration of crystalline gibbsite to form crystalline boehmite led to the precipitation of a nanocrystalline phase which was identified as κ-Al_2O_3 (ICSD #84375) [54]. Some humps arising from aluminum oxide were identified in the Rietveld plot, and the quantitative phase analysis of this sample gave a phase assemblage of 42.4(1) wt% of crystalline boehmite and 57.6(3) wt% of nanocrystalline κ-Al_2O_3. The overall non-crystalline content was determined by internal standard methodology from LXRPD data. The obtained amount for amorphous/nanocrystalline was 67.3(3) wt%. Fig. S2b shows the LXRPD Rietveld plot with the peaks belonging to the internal standard starred.

An initial estimation of the particle size of nanocrystalline κ-Al_2O_3 was obtained by the Scherrer approach [55], see Eq. (6), by using the SXRPD data.

$$\tau = \frac{\kappa\lambda}{\beta\cos\theta} \tag{6}$$

where τ is the mean particle size of the ordered domains, κ is a dimensionless parameter which depends upon the shape of the particles, λ is the employed wavelength, β is the integral breath after subtracting the

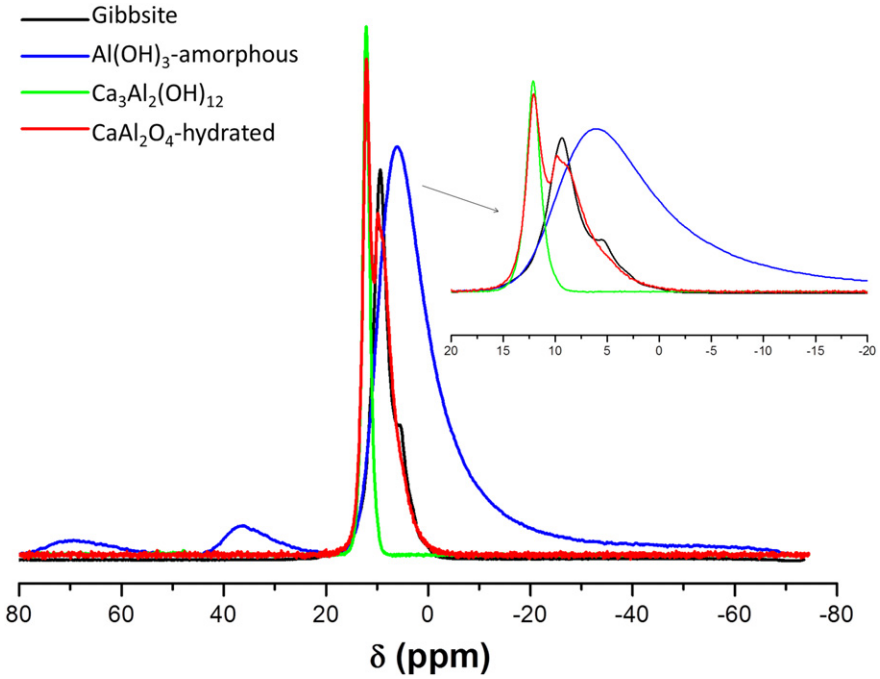

Fig. 3. ^{27}Al MAS-NMR spectra measured at a spinning rate of 15 kHz and a magnetic field of 14.1 T for gibbsite, amorphous $Al(OH)_3$, $Ca_3Al_2(OH)_{12}$ and $CaAl_2O_4$-hydrated.

instrumental line broadening contribution and θ is the Bragg angle of the studied diffraction peak. This study was carried out for the (202) reflection of κ-Al_2O_3, $2\theta = 11.07°$, and $\beta = 0.0117$ rad, and by assuming a κ shape factor of 0.9, the obtained particle size was 3 nm.

The Rietveld analysis of the SXRPD pattern of hydrogarnet was carried out using the crystal structure previously reported [11] as starting model. The optimized unit cell value converged to a = 12.57863(2) Å and V = 1990.22(1) $Å^3$. In addition to the peaks corresponding to $Ca_3Al_2(OH)_{12}$, tiny diffraction peaks from other three phases were observed: $Ca(OH)_2$, $Ca_2Al(OH)_6$-$[(CO_3)_{0.25}(OH)_{0.5}\cdot 2H_2O]$ and $Ca_3Al_2O_6$. The crystal structures of these phases were introduced in the Rietveld control file and their contents were optimized. After refining the atomic parameters for hydrogarnet, the final R_{WP} and R_F values were 4.9 and 2.6%, respectively. The phase contents converged to 97.22(4), 1.51(2), 0.88(2) and 0.40(2) wt% for $Ca_3Al_2(OH)_{12}$, $Ca(OH)_2$, $Ca_2Al(OH)_6$-$[(CO_3)_{0.25}(OH)_{0.5}\cdot 2H_2O]$ and $Ca_3Al_2O_6$, respectively. Table S4 reports the refined final atomic parameters but, as discussed above, this structural description has not been deposited. As in the previous case, the hydrogen position could be refined. Fig. 4a shows the final Rietveld plot. The ^{27}Al MAS-NMR spectrum for hydrogarnet is also reported in Fig. 3 where its resonance is located at 12.1 ppm, as previously reported [56].

Finally, the hydrated $CaAl_2O_4$ paste was also studied. According to reaction (4), this sample should contain a mixture of hydrogarnet and aluminum hydroxide gel. The crystal structures of both hydrogarnet and gibbsite, previously obtained, were used for the Rietveld refinement of this pattern. The diffraction peaks arising from the aluminum hydroxide gel were very broad although they were located as predicted from the gibbsite crystal structure, see inset in Fig. 4b. This clearly shows the nanocrystalline structure of the aluminum hydroxide gel. Some additional peaks were observed in this pattern and they were identified as arising from $Ca_2Al(OH)_6[(CO_3)_{0.5}\cdot 2.5H_2O]$, $Ca_2Al(OH)_6[(CO_3)_{0.25}(OH)_{0.5}\cdot 2H_2O]$ and $CaCO_3$ (calcite).

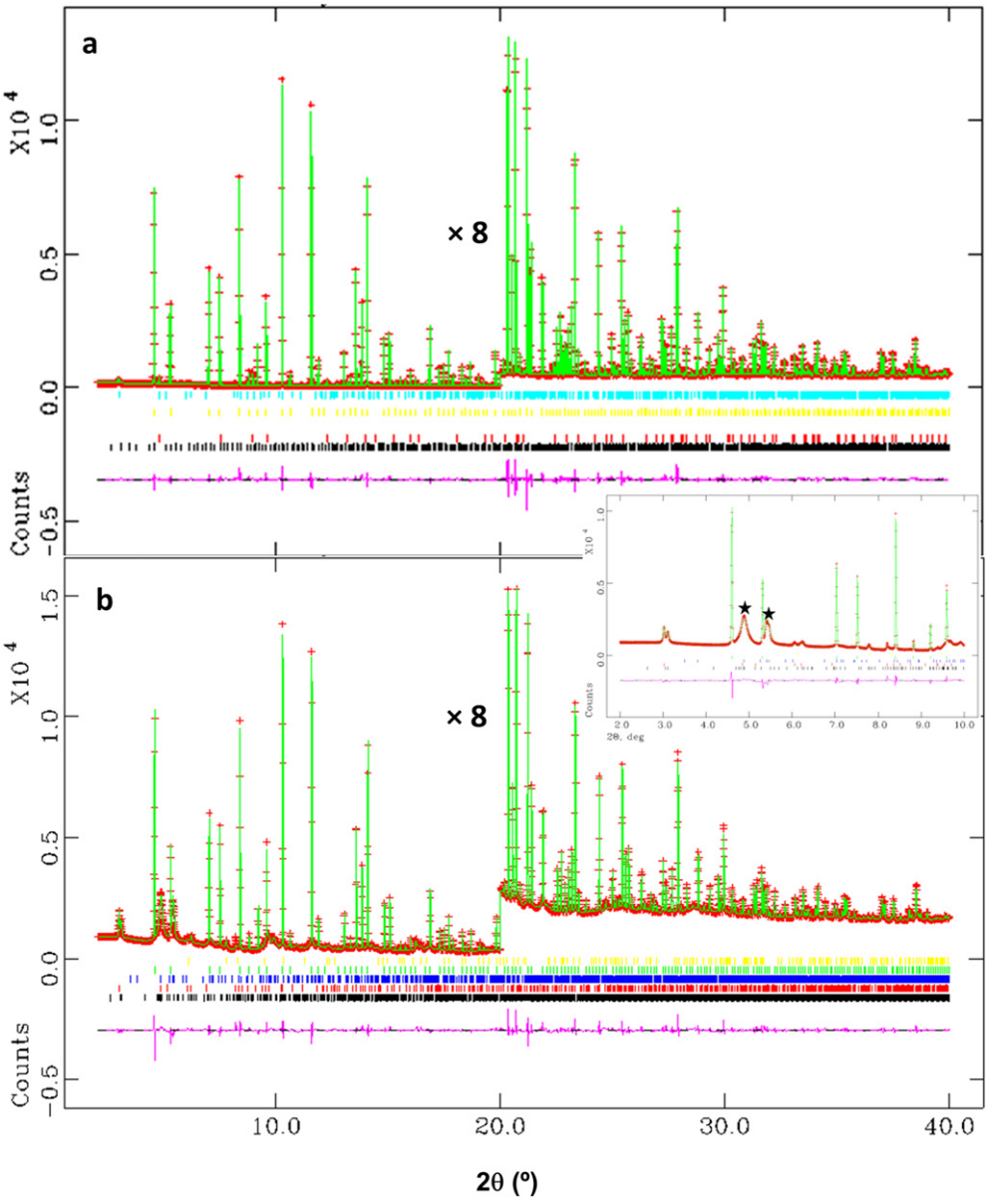

Fig. 4. SXRPD Rietveld plots (λ ~0.41 Å) for (a) hydrogarnet and (b) $CaAl_2O_4$-hydrated. The high angle regions, 20–40° (2θ), have been enlarged by multiplying by a factor (shown above) for a better observation. The bottom inset shows an enlarged view of the low angle region of the hydrated paste, where the gibbsite contribution is highlighted. Tic marks denote the allowed Bragg reflections: in (a) blue for $Ca_3Al_2O_6$, yellow for $Ca(OH)_2$, red for $Ca_3Al_2(OH)_6$ and black for $Ca_2Al(OH)_6$-$[(CO_3)_{0.25}(OH)_{0.5}\cdot 2H_2O]$ and in (b) yellow for $CaCO_3$, green for $Ca_3Al_2(OH)_6$, blue for Al(OH)3, red for $Ca_2Al(OH)_6$-$[(CO_3)_{0.25}(OH)_{0.5}\cdot 2H_2O]$ and black for $Ca_2Al(OH)_6[(CO_3)_{0.5}\cdot 2.5H_2O]$.

The atomic parameters were not refined for the pattern of hydrated $CaAl_2O_4$ paste. The parameters used for this fit were those obtained in the gibbsite and hydrogarnet structural studies. The refined unit cell parameters of the five phases are given in Table S5. The final R_{WP} was 4.7% and the Rietveld plot is displayed in Fig. 4b. The phase contents converged to 43.54(5), 48.0(2), 5.05(9), 2.24(5) and 1.16(6) wt% for $Ca_3Al_2(OH)_{12}$, $Al(OH)_3$, $Ca_2Al(OH)_6[(CO_3)_{0.5}\cdot 2.5H_2O]$, $Ca_2Al(OH)_6$-$[(CO_3)_{0.25}(OH)_{0.5}\cdot 2H_2O]$ and $CaCO_3$, respectively. The ^{27}Al MAS-NMR spectrum for this paste, see Fig. 3, presents only two signals located at 12.0 and 9.5 ppm which correspond to hydrogarnet and gibbsite, respectively. No additional bands were found in other regions.

The Scherrer methodology, see eq. (6), has also been employed for an initial characterization of the particle size of nanocrystalline $Al(OH)_3$ by using the SXRPD data. This study was carried out for the (002) reflection of $Al(OH)_3$, $2\theta = 4.88°$, and $\beta = 0.0042$ rad, and by assuming a κ shape factor of 0.9, the obtained average particle size was 9 nm.

A LXRPD study with internal standard methodology was also carried out for this sample. The crystalline contents were 42.3(4), 2.5(5), 1.7(4) and 2.2(5) wt% for $Ca_3Al_2(OH)_{12}$, $Ca_2Al(OH)_6[(CO_3)_{0.5}\cdot 2.5H_2O]$, $Ca_2Al(OH)_6$-$[(CO_3)_{0.25}(OH)_{0.5}\cdot 2H_2O]$ and $CaCO_3$, respectively. Moreover, the resulting non-crystalline content was 51.3(5) wt%. Fig. S4 displays the corresponding LXRPD Rietveld plot for the hydrated $CaAl_2O_4$ paste. A key conclusion from the SXRPD and LXRPD studies is nanocrystalline nature of the aluminum hydroxide phase with no evidence of an amorphous phase.

3.3. Qualitative PDF study

The raw PDF data for the five reference specimens and the hydrated sample are displayed in Fig. 5. The PDF data for crystalline gibbsite have only the features expected from the crystal structure of gibbsite, including the peaks at 1.91 due to Al—O_{oct}, 2.40 related with Al···H and O···O and 2.85 Å due to Al···Al and O···O interatomic distances. These interatomic distances were calculated from the CIF file using the GSAS software. In addition, the corresponding data for the milled gibbsite show less pronounced interatomic peaks. Peaks below 1.5 Å are considered as termination ripples and they are due to imperfect corrections and termination errors [22]. It is worth pointing out that for data collection issues, the acquisition time for milled gibbsite was lower than that for other compounds and consequently, the quality of the PDF pattern was poorer.

The PDF data for commercial amorphous aluminum hydroxide, see Fig. 5, show the main interatomic peaks corresponding to gibbsite, 1.88, 2.35 and 2.86 Å. However, only interatomic peaks up to a correlation length of ~6 Å are observed. Further characterization of this amorphous sample is out of the scope of this paper.

The PDF data for boehmite show the interatomic peaks at 1.89, 2.55, 2.86 and 3.40 Å due to Al—O_{oct}, Al···H, Al···Al and Al···O interatomic distances, respectively, see Fig. 5. We note that the second and third peaks also contains a contribution from O···O correlations and that the peak at 3.40 Å is characteristic of this oxo-hydroxide phase and it is not present in the aluminum hydroxide phases, see Fig. S5.

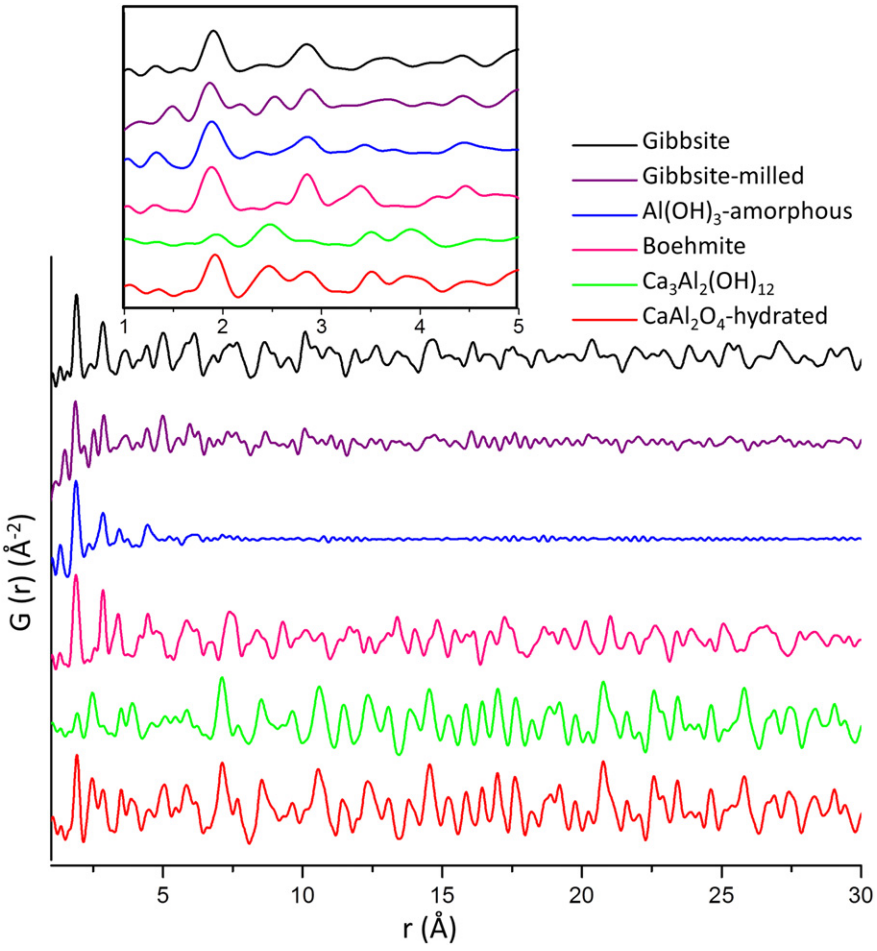

Fig. 5. Experimental PDFs for as-received commercial crystalline gibbsite, milled gibbsite, as-received commercial amorphous aluminum hydroxide, boehmite, $Ca_3Al_2(OH)_{12}$ and hydrated $CaAl_2O_4$ sample.

The PDF data for $Ca_3Al_2(OH)_{12}$, see Fig. 5, have all the features expected from its crystal structure, including the peaks at 1.93, 2.46, 3.50, due to Al—O_{oct}, Ca-O and Ca···Al interatomic distances, respectively and the peak at 3.90 Å related with a mixture of Ca···Ca, Al···O_{oct} and Ca···O.

The PDF data for the hydrated sample, see bottom of Fig. 5, show the expected features for a mixture of hydrogarnet and gibbsite: 1.92, 2.47, 2.85, 3.51 and 3.87 Å. The presence of aluminum oxo-hydroxide (boehmite) is discarded because there are no interatomic peaks in the region of 3.40 Å. Moreover, the signal at 4.17 Å, which is also present in boehmite, it is neither included in this hydrated sample, see Fig. S5.

3.4. Quantitative PDF analysis

Four patterns (commercial crystalline gibbsite, hydrogarnet, boehmite and hydrated calcium aluminate paste) have been quantitatively studied by using the PDFgui software. The main final objective of the study was to quantify the presence of nanocrystalline aluminum hydroxide in the cement paste. For the crystalline samples, commercial crystalline gibbsite and hydrogarnet, the 1.5–10 Å range was selected for the analyses. The final fits of the PDF data for these two samples are displayed in Fig. 6. It is worth noting that we do not report errors in the results as the standard deviations are not properly calculated by PDFgui. This is because the standard data reduction obtained by PDFgetX3 [44] does not include the dG column, standard deviations of G, which is needed to properly calculate the errors.

The PDF data for commercial gibbsite was fitted with the crystal structure determined from the Rietveld study described just above. After optimizing the scale factor, the ADPs values for aluminum and oxygen atoms, the delta2 parameter and the unit cell parameters, the final refinement led to a R_W value of 17.8%. The final fit is displayed in Fig. 6a, the final ADPs values are reported in Table S2 and the unit cell values for gibbsite converged to a = 8.665 Å, b = 5.074 Å, c = 9.765 Å and β = 94.61°.

The PDF data for $Ca_3Al_2(OH)_{12}$ sample was fitted with the crystal structure determined from the Rietveld study, also described just above. In the final refinement, R_W dropped to 15.2% and the $Ca(OH)_2$ content was 1.9 wt%. The contribution to the PDF analysis by $Ca_2Al(OH)_6[(CO_3)_{0.25}(OH)_{0.5}\cdot 2H_2O]$ was tested but it did not improve the fit, therefore it was not considered in the last refinements. The final fit is displayed in Fig. 6b, the final ADPs values are reported in Table S4 and the unit cell value for hydrogarnet converged to a = 12.585 Å.

The PDF data for boehmite is more complex due to the presence of two main phases of different nature. Boehmite is crystalline and aluminum oxide is nanocrystalline. In this case, a different strategy was used for the PDF fit. The crystalline boehmite was fit over a high r region, i.e. 30–50 Å, where no contributions from nano-crystalline or amorphous phases were apparent. The final R_W value was 19.8%. The final fit is displayed in Fig. 7c. The final ADPs values are reported in Table S3 and the unit cell values converged to a = 3.696 Å, b = 12.244 Å, c = 2.866 Å. After this refinement, all the parameters for the boehmite phase were kept fixed and the contribution from nanocrystalline aluminum oxide was refined in a lower region, from 1.5 to 30 Å, see Fig. 7b. In addition, Fig. 7a shows a zoom of the smallest r-range. The final R_W value in this region was 26.7% and the unit cell values for aluminum oxide were a = 4.885 Å, b = 8.429 Å and c = 8.683 Å. Moreover, for nanocrystalline aluminum oxide, spdiameter was also refined converging to 2 nm. Finally, the obtained phase contents were 33.4 wt% for crystalline boehmite and 66.6 wt% for nanocrystalline aluminum oxide.

As the hydrated $CaAl_2O_4$ paste contained crystalline hydrogarnet and nanocrystalline gibbsite, the same strategy explained just above was used here. Initially, the PDF data in the high r-region, 60 to 80 Å, was fitted with the crystal structure of crystalline hydrogarnet, see Fig. 8d. After optimizing the scale factors, unit cell and ADPs, the R_W converged to 14.9%. The unit cell value for hydrogarnet converged to a = 12.581 Å and the final ADPs values obtained for $Ca_3Al_2(OH)_{12}$ were 0.0058, 0.0066 and 0.0174 $Å^2$ for Ca, Al and O, respectively. Subsequently, all the parameters for the crystalline hydrogarnet phase were kept fixed and the r-region, 1.5–60 Å, was used to fit the nanocrystalline aluminum hydroxide gel contribution. After optimizing all the parameters, the scale factors, unit cell parameters, ADPs, delta2, atomic parameters and spdiameter, R_W converged to 21.0%. The final fit is displayed in Fig. 8b and c. In addition, Fig. 8a shows a zoom of the smallest r-range. The unit cell value for gibbsite converged to a = 8.727 Å, b = 5.044 Å, c = 9.609 Å, β = 95.2°. Moreover, the final ADPs values obtained for nanocrystalline gibbsite were 0.0082 and 0.0072 $Å^2$ for Al and O, respectively. The phase contents were 42.0, 52.8 and 5.2 wt% for $Ca_3Al_2(OH)_{12}$, $Al(OH)_3$ and $Ca_2Al(OH)_6[(CO_3)_{0.5}\cdot 2.5H_2O]$, respectively. Chiefly, the spdiameter coefficient for aluminum hydroxide converged to 5.3 nm.

4. Discussion

The SXRPD pattern for commercial amorphous aluminum hydroxide, see Fig. S1, indicates that the sample does not present long range order. The raw PDF data for this amorphous sample, Fig. 5, shows interatomic peaks up to ~0.6 nm. At short interatomic distances, the expected octahedral Al—O and Al···Al peaks, located at 1.88 and 2.86 Å, respectively, are observed. The presence of additional Al—O bonds, likely arising from $Al(OH)CO_3$ has been observed by ^{27}Al MAS-NMR, see Fig. 3. The profile presents a main broad signal around 6.1 ppm which corresponds to octahedral coordination, AlO_6, from amorphous aluminum hydroxide. Moreover, two additional small signals are observed. The band located at 36.4 ppm is likely due to aluminum in pentacoordinated environment(s) [52], AlO_5, and the band centered at 69.4 ppm is due to

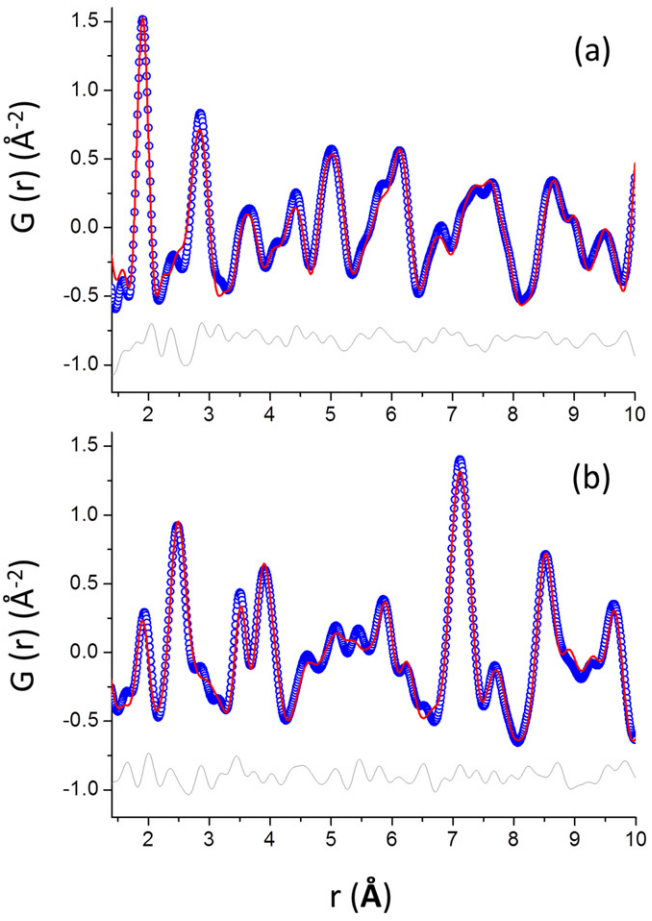

Fig. 6. Experimental (blue circles) and fitted (red solid line) PDFs for (a) gibbsite and (b) $Ca_3Al_2(OH)_{12}$.

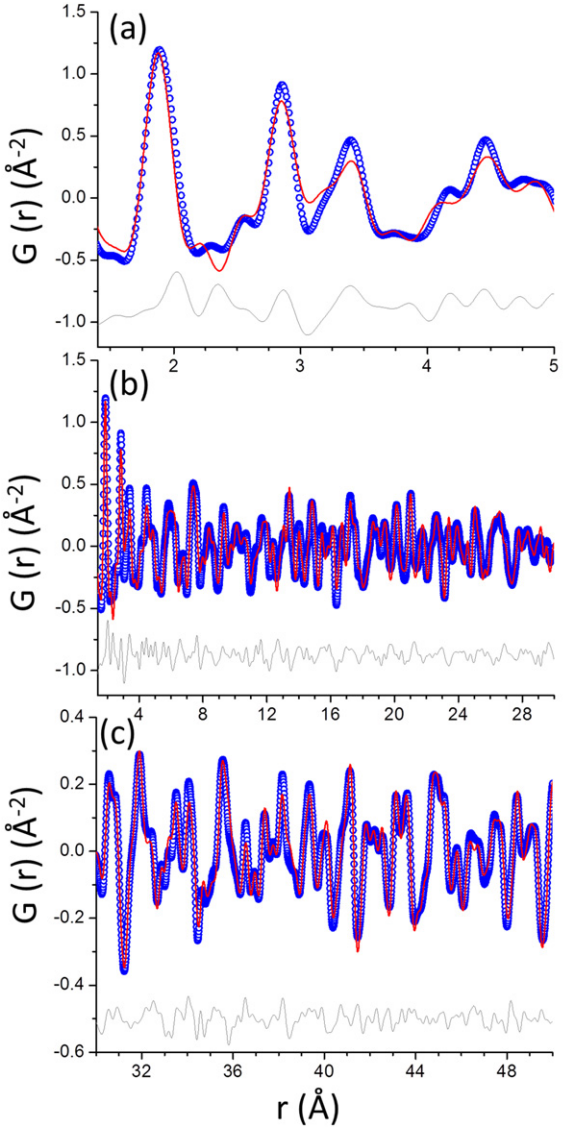

Fig. 7. Experimental (blue circles) and fitted (red solid line) PDFs for boehmite (a) from 1.4 to 5 Å (b) from 1.4 to 30 Å and (c) from 30 to 50 Å.

aluminum(s) in tetrahedral environment(s), AlO_4 [52]. The contribution of this tetrahedral coordination, interatomic distance ~1.75 Å, is not visible in the PDF pattern. We speculate that this is due to its low intensity and being partly overlapped with the main broad interatomic peak of this sample, Al—O_{oct}, which appears at 1.88 Å. Finally, and taking into account the thermal analysis, a stoichiometry close to $Al(OH)_3 \cdot 0.4H_2O$ was deduced for this sample which also contains about 12 wt% of $Al(OH)CO_3$.

Concerning the $Al(OH)_3$ reference materials, the Rietveld analysis of the commercial crystalline gibbsite sample showed that it contains one crystalline phase. The determination of the non-crystalline content by using the internal standard methodology gave a value close to zero. Therefore, this study indicated that the amorphous content in the commercial crystalline gibbsite sample was negligible. In addition, the Rietveld analysis of the powder pattern of milled gibbsite also indicated the presence of one crystalline phase. However, the low quality of the PDF pattern does not allow us to perform an adequate quantitative study for this sample.

Regarding the $Ca_3Al_2(OH)_{12}$ reference sample, it is worth highlighting the agreement between the phase composition determined from Rietveld analysis and PDF investigation. The crystalline $Ca(OH)_2$ content was determined to be 1.51(2) wt% by Rietveld methodology in very good agreement with an overall $Ca(OH)_2$ content of 1.9 wt% obtained by PDF calculations. Finally, it has been found heterogeneity in this sample and some regions contained significant amount of the pristine anhydrous phase, $Ca_3Al_2O_6$. This could justify that the measured overall weight loss, 26.3 wt%, was slightly lower than the expected theoretical value, 28.5 wt%. However, we noted that only a small amount of

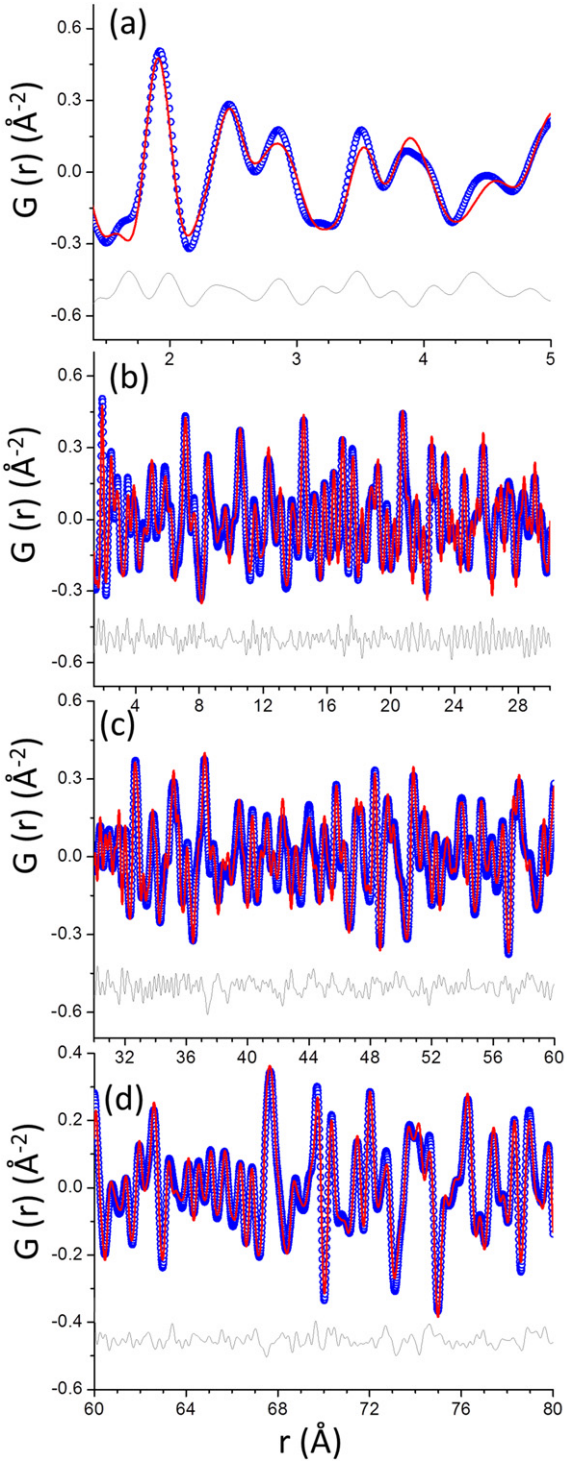

Fig. 8. Experimental (blue circles) and fitted (red solid line) PDFs for $CaAl_2O_4$-hydrated sample (a) from 1.4 to 5 Å, (b) from 1.4 to 30 Å (c) from 30 to 60 Å and (d) from 60 to 80 Å.

$Ca_3Al_2O_6$ was detected in the scanned region of the capillary used for acquiring the synchrotron powder diffraction pattern.

On the one hand, boehmite was studied as a reference material in order to highlight the differences with crystalline gibbsite. The characteristic bands of boehmite allow discarding its presence in the $CaAl_2O_4$ hydrated sample. On the other hand, a different protocol was followed to fit the PDF patterns of a mixture of crystalline and nanocrystalline phases [5]. Although the Rietveld methodology is not likely the best strategy to fit nanocrystalline phases with small particle sizes, the quantitative phase analysis was performed as an initial approximation which yielded 57.6 wt% of aluminum oxide and 42.4 wt% of boehmite. The quantitative results obtained by using PDF data are in good agreement. The PDF analysis of boehmite sample gave 66.6 wt% of aluminum oxide, with an average particle size of ~2 nm, and 33.4 wt% of crystalline boehmite. The particle size obtained by SXRPD data using the Scherrer Eq. (6), 3 nm, is very close to that obtained by using the PDF methodology. Moreover, the total amount of non-crystalline material (amorphous and nanocrystalline) was determined through the internal standard methodology. This study gave a 32.7(3) wt% of boehmite and a 67.3(3) wt% of amorphous and nanocrystalline content. The agreement of this value with the amount of nanocrystalline κ-Al_2O_3 content determined by PDF analysis, 66.6 wt%, indicates that the amorphous content of the sample is negligible.

Finally, we focus on the study of the $CaAl_2O_4$ hydrated sample containing the nanocrystalline aluminum hydroxide gel. The stoichiometric hydration reaction of $CaAl_2O_4$ to yield both $Ca_3Al_2(OH)_{12}$ and stoichiometric non-hydrated $Al(OH)_3$ should theoretically give a sample with 54.8 wt% of hydrogarnet and 45.2 wt% of gibbsite. Both Rietveld and PDFs analyses yielded quantitative phase contents with a lower amount of hydrogarnet than gibbsite, 43.5 and 48.0 wt% (by Rietveld), 42.0 and 52.8 wt% (by PDF), respectively. Firstly, it must be noted the excellent agreement between the Rietveld and the PDF results, chiefly considering the nanocrystalline nature of the aluminum hydroxide component. Secondly, 5.05(9) wt% of $Ca_2Al(OH)_6[(CO_3)_{0.5}\cdot 2.5H_2O]$ and 2.24(5) wt% of $Ca_2Al(OH)_6[(CO_3)_{0.25}(OH)_{0.5}\cdot 2H_2O]$ was determined by Rietveld methodology and 5.2 wt% of $Ca_2Al(OH)_6[(CO_3)_{0.5}\cdot 2.5H_2O]$ was determined by PDF approach. The agreement between these two determinations is outstanding and shows the high accuracy of the PDF phase analysis. Furthermore, the accuracy of the reported data allows explaining the apparent disagreement between the expected and measured hydrogarnet/gibbsite ratio. As the hydrated sample contained mono (and hemicarbonate) phases which have higher Ca/Al ratios, larger amounts of aluminum hydroxide are needed for mass balance. Therefore, the presence of these phases justifies the higher than expected measured gibbsite content. The average size of the gibbsite nanoparticles was found to be close to 5.3 nm from the quantitative PDF study. The obtained value by using the Scherrer approach was a bit larger, 9 nm. Finally, it is important to point out that the LXRPD study using the internal standard methodology gave a value for the non-crystalline content of 51.3(5) wt%. The closeness of this value with the nanocrystalline aluminum hydroxide content determined by PDF, 52.8 wt%, indicates that the amorphous content is also negligible.

An electron microscopy study has also been carried out to determine the possible calcium content of nanocrystalline aluminum hydroxide particles in $CaAl_2O_4$-hydrated sample [14]. These aluminum hydroxide nanoparticles were unstable under the electron beam. Therefore a fast HRTEM study was carried out and, as an example, a HRTEM image of an isolated nanoparticle is displayed in Fig. 9. This Figure also shows the Al/Ca mapping. The results from 20 analyzed aluminum hydroxide nanoparticles yielded 97.7(9) and 2.3(8) at% for Al and Ca contents,

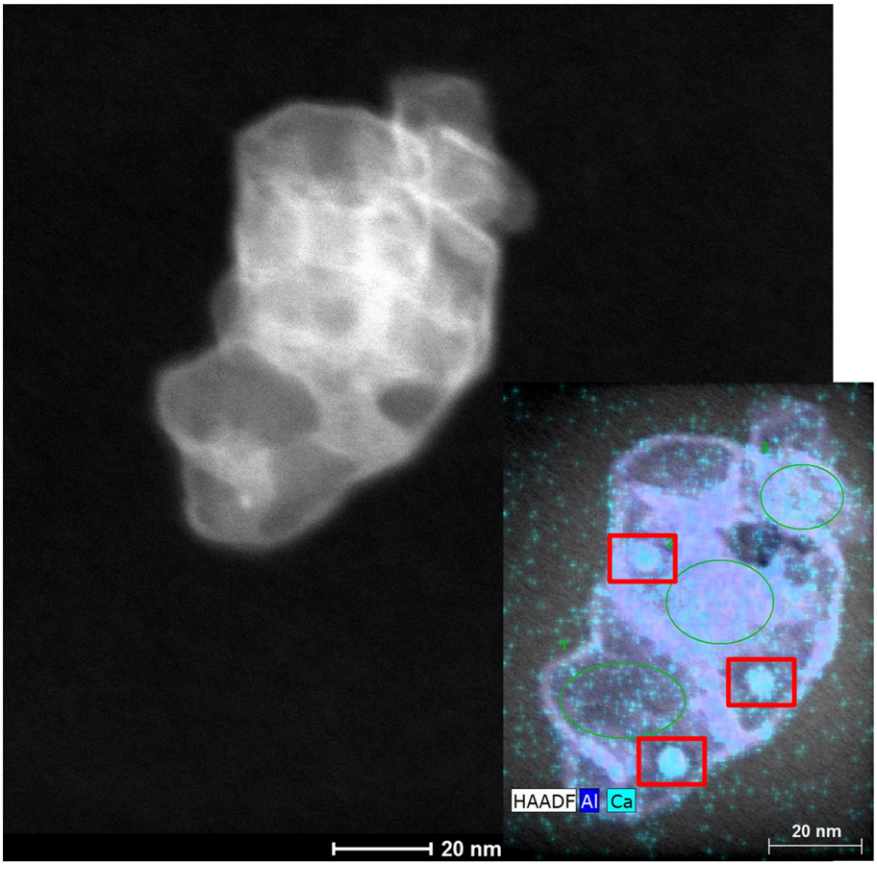

Fig. 9. HRTEM micrograph of an aluminum hydroxide gel nanoparticle presents in the hydrated sample. The cation distribution mapping, Al and Ca, is also shown. The red boxes highlight very small Ca slightly-rich nanoparticles, with sizes close to 4–5 nm.

respectively. It can be seen that there are very small particles, smaller than 4–5 nm, which contain a bit of calcium. This could be explained as trapped hydrogarnet nanoparticles as previously reported for aluminum hydroxide gels from calcium sulfoaluminate cements [14].

Finally, although crystalline (or nanocrystalline) gibbsite does not contain hydration water, small nanoparticles may enclose tiny channels where water molecules can be located interacting with the outer surface of the pack of layers. This is sometimes referred as 'inter-nanoparticle water'. This water is different from the 'free water' concept of cement pastes as it cannot be easily released. Since the phase assemblage of $CaAl_2O_4$-hydrated sample was accurately determined by Rietveld and PDF analyses as 42.1, 49.6, 5.0, 2.2 and 1.1 wt% for $Ca_3Al_2(OH)_{12}$, $Al(OH)_3$, $Ca_2Al(OH)_6[(CO_3)_{0.5}\cdot 2.5H_2O]$, $Ca_2Al(OH)_6[(CO_3)_{0.25}(OH)_{0.5}\cdot 2H_2O]$ and $CaCO_3$, it is possible to estimate the water content that strongly interacts with the layers of nanocrystalline gibbsite. It can be performed by considering the overall water loss of this sample, 32.7 wt% and the theoretical water loss of all components, 31.7 wt%. This easy calculation yields a composition close to $Al(OH)_3\cdot 0.1H_2O$ for the aluminum hydroxide gel formed in the reported hydration conditions, 50 °C. We are aware that lower hydration temperatures lead to nanocrystalline aluminum hydroxide gels with smaller particle sizes that may contain more inter-nanoparticle water. Under certain conditions, amorphous aluminum hydroxide gel could be formed. It is also worth noting that the temperature of the water loss of hydrogarnet phase in the cement phase, 290 °C, is quite close to that measured in highly crystalline hydrogarnet sample, 300 °C. Conversely, the temperature of the water loss of the nanocrystalline gibbsite phase in the cement phase, 260 °C, is significantly lower than that measured in crystalline gibbsite sample, 295 °C, as expected [48].

5. Conclusions

Firstly, commercial crystalline gibbsite is a single phase and the use of Rietveld, PDF and density measurements indicates that its amorphous content was very low, if any. Secondly, commercial amorphous aluminum hydroxide had a complex PDF profile with very small scattering domains with size close to 0.6 nm. The thermal analysis revealed a very significant release of CO_2 and the characterization techniques point towards a large content, close to 12 wt%, of amorphous $Al(OH)CO_3$. Thirdly, the PDF pattern of a mixture of crystalline boehmite and nanocrystalline aluminum oxide was properly fit by performing a two-stage study in different regions: a high-r region was employed for analyzing the crystalline phase and a low-r region was used for analyzing the mixture of crystalline and nanocrystalline phases. The average size of aluminum oxide nanoparticles was found to be around 2 nm. Finally, the key hydrated aluminate paste mainly contained crystalline $Ca_3Al_2(OH)_{12}$ and nanocrystalline gibbsite gel, 43 and 50 wt%, respectively. The LXRPD study with internal standard methodology ruled out the presence of amorphous content in this paste. The aluminum hydroxide gel composition has been determined as $Al(OH)_3\cdot 0.1H_2O$ which takes into account the strongly interacting inter-nanoparticle water. The PDF analysis revealed that this gel has a gibbsite local structure with an average nanoparticle size close to 5 nm. Finally, the accuracy of the phase contents determined from PDF analyses has been established by the agreement with the corresponding values determined from the Rietveld study and the internal standard methodology.

Acknowledgements

This work has been supported by Spanish MINECO through BIA2014-57658-C2-1-R and BIA2014-57658-C2-2-R, which is co-funded by FEDER, research grants. R.U.I. acknowledges funding of CNPQ, grant no. 206983/2014-0/SWE. We also thank CELLS-ALBA (Barcelona, Spain) for providing synchrotron beam time at BL04-MSPD and Dr. Oriol Vallcorba for his assistance during the synchrotron experiment.

Appendix A. Supplementary data

Supplementary data to this article can be found online at http://dx.doi.org/10.1016/j.cemconres.2017.02.025.

References

[1] A. Violante, P.M. Huang, Formation mechanism of aluminum hydroxide polymorphs, Clay Clay Miner. 41 (1993) 590–597.
[2] I. Levin, D. Brandon, Metastable alumina polymorphs: crystal structures and transition sequences, J. Am. Ceram. Soc. 81 (1998) 1995–2012.
[3] R. Demichelis, M. Catti, R. Dovesi, Structure and stability of the $Al(OH)_3$ polymorphs doyleite and nordstrandite: a quantum mechanical ab initio study with the CRYSTAL06 code, J. Phys. Chem. C 113 (2009) 6785–6791.
[4] A.D.V. Souza, C.C. Arruda, L. Fernandes, M.L.P. Antunes, P.K. Kiyohara, R. Salomão, Characterization of aluminum hydroxide ($Al(OH)_3$) for use as a porogenic agent in castable ceramics, J. Eur. Ceram. Soc. 35 (2015) 803–812.
[5] C.E. White, L.L. Daemen, H. Monika, P. Katharine, Intrinsic differences in atomic ordering of calcium (alumino)silicate hydrates in conventional and alkali-activated cements, Cem. Concr. Res. 67 (2015) 66–73.
[6] H. Pöllmann, Calcium aluminate cements – raw materials, differences, hydration and properties, Rev. Mineral. Geochem. 74 (2012) 1–82.
[7] H.F.W. Taylor, Cement Chemistry, Thomas Telford, London, 1997.
[8] S. Rashid, P. Barnes, J. Bensted, X. Turrillas, Conversion of calcium aluminate cement hydrates re-examined with synchrotron energy-dispersive diffraction, J. Mater. Sci. Lett. 13 (1994) 1232–1234.
[9] X. Liu, M.A.G. Aranda, B. Chen, P. Wang, R. Harder, I. Robinson, In situ Bragg coherent diffraction imaging study of a cement phase microcrystal during hydration, Cryst. Growth Des. 15 (2015) 3087–3091.
[10] K.L. Scrivener, A. Capmas, Calcium aluminate cements, in: P.C. Hewlett (Ed.), Leás Chemistry of Cement and Concrete, fourth ed.Arnold, London 1998, pp. 723–727 (Chapter 13).
[11] F. Guirado, S. Galí, S. Chinchón, J. Rius, Crystal structure solution of hydrated high-alumina cement from X-ray powder diffraction data, Angew. Chem. Int. Ed. 37 (1998) 72–75.
[12] G.A. Lager, T.H. Armbruster, J. Faber, Neutron and X-ray diffraction study of hydrogarnet $Ca_3Al_2(O_4H_4)_3$, Am. Mineral. 72 (1987) 756–765.
[13] F. Winnefeld, S. Barlag, Calorimetric and thermogravimetric study on the influence of calcium sulfate on the hydration of ye'elimite, J. Therm. Anal. Calorim. 101 (2010) 949–957.
[14] F. Song, Z. Yu, F. Yang, Y. Lu, Y. Liu, Microstructure of amorphous aluminum hydroxide in belite-calcium sulfoaluminate cement, Cem. Concr. Res. 71 (2015) 1–6.
[15] J. Bizzozero, C. Gosselin, K.L. Scrivener, Expansion mechanisms in calcium aluminate and sulfoaluminate systems with calcium sulfate, Cem. Concr. Res. 56 (2014) 190–202.
[16] L. Pelletier, F. Winnefeld, B. Lothenbach, The ternary system Portland cement-calcium sulphoaluminate clinker-anhydrite: hydration mechanism and mortar properties, Cem. Concr. Compos. 32 (2010) 497–507.
[17] J.M. Rivas-Mercury, X. Turrillas, A.H. De Aza, P. Pena, Calcium aluminates hydration in presence of amorphous SiO_2 at temperatures below 90 °C, J. Solid State Chem. 179 (2006) 2988–2997.
[18] M.A.G. Aranda, A.G. De la Torre, L. Leon-Reina, Rietveld quantitative phase analysis of OPC clinkers, cements and hydration products, Rev. Mineral. Geochem. 74 (2012) 169–209.
[19] K.L. Scrivener, T. Fullmann, E. Gallucci, G. Walenta, E. Bermejo, Quantitative study of Portland cement hydration by X-ray diffraction/Rietveld analysis and independent methods, Cem. Concr. Res. 34 (2004) 1541–1547.
[20] L.D. Mitchell, J.C. Margeson, P.S. Whitfield, Quantitative Rietveld analysis of hydrated cementitious systems, Powder Diffract. 21 (2006) 111–113.
[21] G. Álvarez-Pinazo, A. Cuesta, M. García-Maté, A.G. De la Torre, L. León-Reina, M.A.G. Aranda, Rietveld quantitative phase analysis of Yeelimite-containing cements, Cem. Concr. Res. 42 (2012) 960–971.
[22] T. Egami, S.J.L. Billinge, Underneath the Bragg-Peaks: Structural Analysis of Complex Materials, second ed. Elsevier, Amsterdam, 2012.
[23] M.A.G. Aranda, Recent studies of cements and concretes by synchrotron radiation crystallographic and cognate methods, Crystallogr. Rev. 22 (2016) 150–196.
[24] S. Soyer-Uzun, S.R. Chae, C.J. Benmore, H.-R. Wenk, P.J.M. Monteiro, Compositional evolution of calcium silicate hydrate (C-S-H) structures by total X-ray scattering, J. Am. Ceram. Soc. 95 (2012) 793–798.
[25] L.B. Skinner, S.R. Chae, C.J. Benmore, H.R. Wenk, P.J.M. Monteiro, Nanostructure of calcium-silicate-hydrates in cements, Phys. Rev. Lett. 104 (2010) 195502.
[26] C. Meral, C.J. Benmore, P.J.M. Monteiro, The study of disorder and nanocrystallinity in C-S-H, supplementary cementitious materials and geopolymers using pair distribution function analysis, Cem. Concr. Res. 41 (2011) 696–710.
[27] C.E. White, P. Katharine, N.J. Henson, J.L. Provis, In situ synchrotron X-ray pair distribution function analysis of the early stages of gel formation in metakaolin-based geopolymers, Appl. Clay Sci. 73 (2013) 17–25.
[28] M.E. Natali, C.E. White, M.C. Bignozzi, Elucidating the atomic structures of different sources of fly ash using X-ray and neutron PDF analysis, Fuel 177 (2016) 148–156.
[29] S.J.L. Billinge, M.G. Kanatzidis, Beyond crystallography: the study of disorder, nanocrystallinity and crystallographically challenged materials with pair distribution functions, Chem. Commun. (2004) 749–760.

[30] T. Proffen, K.L. Page, S.L. McLain, B. Clausen, T.W. Darling, J.A. TenCate, S.-Y. Lee, E. Ustandag, Atomic pair distribution function analysis of materials containing crystalline and amorphous phases, Z. Kristallogr. 220 (2005) 1002–1008.
[31] T. Davis, M. Johnson, S.J.L. Billinge, Towards phase quantification at the nanoscale using the total scattering pair distribution function (TSPDF) method: recrystallization of cryomilled sulfamerazine, Cryst. Growth Des. 13 (2013) 4239–4244.
[32] D. Prill, P. Juhas, M.U. Schmidt, S.J.L. Billinge, Modeling pair distribution functions (PDF) of organic compounds: describing both intra- and intermolecular correlation functions in calculated PDFs, J. Appl. Crystallogr. 48 (2015) 171–178.
[33] M.W. Terban, E.Y. Cheung, P. Krolikowski, S.J.L. Billinge, Recrystallization phase composition and local structure of amorphous lactose from the total scattering pair distribution function, Cryst. Growth Des. 16 (2015) 210–220.
[34] S. Thakral, M.W. Terban, N.K. Thakral, R. Suryanarayanan, Recent advances in the characterization of amorphous pharmaceuticals by X- ray diffractometry, Adv. Drug Deliv. Rev. 100 (2016) 183–193.
[35] M.W. Terban, M. Johnson, M.D. Michiel, S.J.L. Billinge, Detection and characterization of nanoparticles in suspension at low concentrations using the x-ray total scattering pair distribution function technique, Nano 7 (2015) 5480–5487.
[36] W. Li, R. Harrington, Y. Tang, J.D. Kubicki, M. Aryanpour, R.J. Reeder, J.B. Parise, B.L. Phillips, Differential pair distribution function study of the structure of arsenate adsorbed on nanocrystalline γ-alumina, Environ. Sci. Technol. 45 (2011) 9687–9692.
[37] S. Brühe, S. Gottlieb, W. Assmus, E. Alig, M.U. Schmidt, Atomic structure analysis of nanocrystalline boehmite AlO(OH), Cryst. Growth Des. 8 (2008) 489–493.
[38] G. Paglia, E.S. Bozin, S.J.L. Billinge, Fine-Scale Nanostructure in γ-Al_2O_3, Chem. Mater. 18 (2006) 3242–3248.
[39] L. Samain, A. Jaworski, M. Edén, D.M. Ladd, D.K. Seo, F.J. Garcia-Garcia, U. Häussermann, Structural analysis of highly porous γ-Al_2O_3, J. Solid State Chem. 217 (2014) 1–8.
[40] M. García-Mate, A.G. De la Torre, L. Leon-Reina, M.A.G. Aranda, I. Santacruz, Hydration studies of calcium sulfoaluminate cements blended with fly ash, Cem. Concr. Res. 54 (2013) 12–20.
[41] F. Fauth, I. Peral, C. Popescu, M. Knapp, The new material science powder diffraction beamline at ALBA synchrotron, Powder Diffract. 28 (2013) S360–S370.
[42] A.G. De la Torre, S. Bruque, M.A.G. Aranda, Rietveld quantitative amorphous content analysis, J. Appl. Crystallogr. 34 (2001) 196–202.
[43] A.C. Larson, R.B. Von Dreele, General Structure Analysis System (GSAS), Los Alamos National Laboratory Report LAUR, 2000 86–748.
[44] P. Juhàs, T. Davis, C.L. Farrow, S.J.L. Billinge, PDFgetX3: a rapid and highly automatable program for processing powder diffraction data into total scattering pair distribution functions, J. Appl. Crystallogr. 46 (2013) 560–566.
[45] C.L. Farrow, P. Juhás, J. Liu, D. Bryndin, E.S. Božin, J. Bloch, T. Proffen, S.J.L. Billinge, PDFfit2 and PDFgui: computer programs for studying nanostructure in crystals, J. Phys. Condens. Matter 19 (2007) 335219.
[46] I.-K. Jeong, T. Proffen, F. Mohiuddin-Jacobs, S.J.L. Billinge, Measuring correlated atomic motion using X-ray diffraction, J. Phys. Chem. A 103 (1999) 921–924.
[47] I.-K. Jeong, R.H. Heffner, M.J. Graf, S.J.L. Billinge, Lattice dynamics and correlated atomic motion from the atomic pair distribution function, Phys. Rev. B 67 (2003) 104301.
[48] T. Tsuchida, N. Ichikawa, Mechanochemical phenomena of gibbsite, bayerite and boehmite by grinding, React. Solids 7 (1989) 207–217.
[49] H.G. Midgley, Determination of calcium hydroxide in set Portland cements, Cem. Concr. Res. 9 (1979) 77–82.
[50] H. Saalfeld, M. Wedde, Refinement of the crystal structure of gibbsite, $Al(OH)_3$, Z. Kristallogr. 139 (1974) 129–135.
[51] J. Skibsted, E. Henderson, H. Jakobsen, Characterization of calcium aluminate phases in cements by aluminum-27 MAS NMR spectroscopy, J. Inorg. Chem. 32 (1993) 1013–1027.
[52] T. Isobe, T. Watanabe, J.B. d'Epinose de la Caillerie, A.P. Legrand, D. Massiot, Solid-state ^{1}H and ^{27}Al NMR studies of amorphous aluminum hydroxides, J. Colloid Interface Sci. 261 (2003) 320–324.
[53] G.G. Christoph, C.E. Corbato, A. Hofmann, R.T. Tettenhorst, The crystal structure of boehmite, Clay Clay Miner. 27 (1979) 81–86.
[54] B. Ollivier, R. Retoux, P. Lacorre, D. Massiot, G. Ferey, Crystal structure of κ-alumina: an X-ray powder diffraction, TEM and NMR study, J. Mater. Chem. 7 (1997) 1049–1056.
[55] A. Patterson, The Scherrer formula for X-ray particle size determination, Phys. Rev. 56 (1939) 978–982.
[56] J.M. Rivas-Mercury, P. Pena, A.H. De Aza, X. Turrillas, I. Sobrados, J. Sanz, Solid-state ^{27}Al and ^{29}Si NMR investigations on Si-substituted hydrogarnets, Acta Mater. 55 (2007) 1183–1191.